Evolution of anisotropy with saturation and its implications for the elastoplastic responses of clay rocks

Sabrina C.Y. Ip[1] · Ronaldo I. Borja[1,*]

[1]Department of Civil and Environmental Engineering, Stanford University, Stanford, CA 94305, USA. *E-mail: borja@stanford.edu

Summary. Many clay rocks have distinct bedding planes. Experimental studies have shown that their mechanical properties evolve with the degree of saturation, often with higher stiffness and strength after drying. For transversely isotropic rocks, the effects of saturation can differ between the bed-normal and bed-parallel directions, which gives rise to saturation-dependent stiffness and strength anisotropy. Accurate prediction of the mechanical behavior of clay rocks under partially saturated conditions requires numerical models that can capture the evolving elastic and plastic anisotropy with degree of saturation. In this study, we present an anisotropy framework for coupled solid deformation-fluid flow in unsaturated elastoplastic media. We incorporate saturation-dependent strength anisotropy into an anisotropic modified Cam-Clay model and consider the evolving anisotropy in both the elastic and plastic responses. The model was calibrated using experimental data from triaxial tests to demonstrate its capability in capturing strength anisotropy at various levels of saturation. Through numerical simulations, we demonstrate the role of evolving stiffness and strength anisotropy in the mechanical behavior of clay rocks. Plane strain simulations of triaxial compression tests were also conducted to demonstrate the impacts of material anisotropy and degree of saturation on the mechanical and fluid flow responses.

Keywords. Anisotropy, rock strength, transverse isotropy, unsaturated rock mechanics

1 Introduction

Many rocks exhibit anisotropy in both their mechanical deformation and fluid flow behaviors [7, 25, 29, 41, 56, 94, 98]. Failure to consider this aspect could lead to large errors in the prediction of their hydro-mechanical responses [6, 28, 57, 96]. Mechanical anisotropy in rocks mainly arises from the presence of cleavage, micro-cracks, and bedding planes [12, 39, 70]. In shales, the

This is the author manuscript accepted for publication and has undergone full peer review but has not been through the copyediting, typesetting, pagination and proofreading process, which may lead to differences between this version and the Version of Record. Please cite this article as doi: 10.1002/nag.3289

alignment of anisotropic clay particles, minerals and/or cracks along bedding planes can bring about a strong transversely isotropic behavior [37, 48, 52, 81].

Transverse isotropy is a common type of anisotropy in which the material properties are symmetric about a bedding plane and anisotropic in the direction normal to this plane [14, 50, 66, 103, 107]. The effect of anisotropy on the stiffness and strength of various transversely isotropic rocks has been extensively investigated in the literature [9, 13, 58, 63, 68, 69, 77, 86]. The stiffness and strength of transversely isotropic rocks depend on the direction of the load with respect to the orientation of the bedding plane, and are often different in the bed-normal (BN) and bed-parallel (BP) directions. The maximum strength can occur in either direction, but the minimum strength typically occurs when the load is inclined with the bedding plane, often at an angle θ between 20 and 40° [54]. In addition, the shape of the plot of strength versus bedding plane orientation can be classified as U-shaped type, undulatory type, and shoulder type [70]. These three curve shapes have been associated with different types of discontinuities present in the rock. A single plane of anisotropy, for instance, a joint plane or bedding plane, produces a shoulder type anisotropy curve, while a set of discontinuities such as lamination or cleavage produces a U-shaped anisotropy with no shoulder [2, 70]. On the other hand, undulatory type curves arise from the presence of multiple sets of discontinuity.

The behavior of clay rocks subjected to dessication and hydration processes have been studied in the literature [21, 60, 61, 80, 104]. In some clay-rich shales, these processes have been observed to induce changes in the degree of mechanical anisotropy [36, 49]. Mechanical anisotropy has been shown to be saturation-dependent in these rocks, with the anisotropy ratio generally increasing as the shale dehydrates [55, 87, 101, 104]. The Young's modulus and compressive strength were found to be more sensitive to the degree of saturation in the BP direction [40, 99, 101, 104]. The fracture pattern and failure mode observed in triaxial tests have also been noted to depend on the degree of saturation for certain bedding plane orientations [87]. As a result, saturation-dependent mechanical anisotropy may affect the swelling and shrinkage behavior of rocks. In applications involving wetting and/or drying processes, such as tunnel construction and underground storage of nuclear waste, saturation-dependent mechanical anisotropy must be incorporated in the constitutive modeling of rock behavior.

Many hydromechanical models in the unsaturated range have been developed to model porous media subjected to drying and wetting process [16, 23, 26, 27, 42, 44, 64, 73, 89, 95, 108]. Some of these models [24, 45, 75] extend the modified Cam Clay (MCC) model [82, 83] or the Barcelona Basic Model (BBM) [1] to account for the mechanical behavior of partially saturated materials. Various authors have further extended these plasticity models to account for the effects of evolving anisotropy [3, 74, 91]. Some extensions introduced an anisotropic response through a scalar parameter α, proposed by Dafalias [32–34]. The parameter α is a measure of the degree of plastic

anisotropy that defines the size and inclination of the yield surface. Stropeit et al. [84] extended the S-CLAY1 anisotropic critical state model [91], which uses α to describe anisotropic response into the unsaturated regime by incorporating the BBM framework [1]. D'Onza et al. [38] and Al-Sharrad and Gallipoli [4] further enhanced this model with the aims of improving yield stress and shear strain predictions, respectively. Other studies [79, 90] have also introduced the orientation of the yield surface through a kinematic hardening variable tensor as proposed in Kavvadas [53].

The majority of these aforementioned constitutive models were developed to capture unsaturated soil behaviors. In particular, unsaturated soft clays exhibit an evolving anisotropy induced by plastic strain, in which plastic deformation erases or enhances the degree of plastic anisotropy [5, 74]. Hence, many of these models adopt a rotational hardening law to capture the evolution of the inclination of the yield surface with plastic strain [3, 35, 74, 79, 90, 97]. To incorporate the effects of partial saturation, the evolution of the hardening variables, including the rate of rotation of the yield surface, were made to depend on the suction stress and degree of saturation. However, experimental evidence suggests that clay-rich shales exhibit inherent plastic anisotropy [55, 101, 104]. As a result, the elasto-plastic models mentioned above may not be appropriate for modeling inherently anisotropic rocks. Instead, alternative methods to incorporate anisotropy in the MCC model should be explored when modeling rocks with an evolving anisotropy.

Notable contributions to the constitutive modeling of inherently anisotropic geomaterials were those of Nova [65] and Crook et al. [31], who extended the Cam-Clay model and the MCC model, respectively, to transversely isotropic materials by using a fourth-order projection tensor to rotate the yield surface. For an anisotropic yield surface, the fourth-order projection tensor transforms the Cauchy stress tensor in real space to a fictitious space where the yield surface can be expressed in an isotropic form. More recently, Semnani et al. [76] developed an anisotropic thermoplastic model by also adopting a fourth-order projection tensor to rotate the yield surface. The applications and capabilities of this model can be found in [19, 105, 109–111]; however, these models do not account for an evolving plastic anisotropy induced by partial saturation.

This paper attempts to capture the effects of inherent saturation-dependent plastic anisotropy in clay rocks through an anisotropic elastoplastic model for unsaturated porous media. We extend the constitutive theory presented by Semnani et al. [76] to the unsaturated regime using a compressibility framework proposed by Sitarenios and Kavvadas [78], under the assumption of infinitesimal deformation. Subsequently, we calibrate the model using experimental data on Tournemire shale from Vales et al. [87] and demonstrate its capability in capturing mechanical responses associated with saturation-dependent plastic anisotropy in clay rocks. Finally, stress-point and boundary value simulations were conducted to investigate the combined effects of partial saturation and anisotropy on rock behavior. We note that the effects of the complex multiscale structure of shale were not included in this study.

2 Theory

This section briefly describes the hydromechanical elastoplastic framework adopted in this work. The basis of the framework is the formulation by Zhao and Borja [110, 111] for anisotropic elastoplastic porous materials with compressible grains, which is herein extended to the unsaturated range. The discussion is limited to inherently anisotropic materials undergoing infinitesimal deformation.

2.1 The Biot and Terzaghi effective stresses

In the unsaturated range, two effective stresses emerge from the first law of thermodynamics: the Biot effective stress $\boldsymbol{\sigma}'$ that is conjugate to the elastic component of solid deformation, and the Terzaghi effective stress $\boldsymbol{\sigma}''$ that is conjugate to the plastic component. Assuming the air pressure is atmospheric (passive condition), and using the continuum mechanics convention for the stresses (tension is positive), the two effective stresses take the form

$$\boldsymbol{\sigma}' = \boldsymbol{\sigma} + \psi^w p \boldsymbol{b}\,, \qquad \boldsymbol{\sigma}'' = \boldsymbol{\sigma} + \psi^w p \mathbf{1}\,, \tag{1}$$

where $\boldsymbol{\sigma}$ is the total Cauchy stress tensor, ψ^w is the degree of saturation, p is the pore water pressure, $\mathbf{1}$ is the second-order identity tensor (Kronecker delta), and $\boldsymbol{b}$ is the Biot tensor. In the Biot effective stress, the pressure term is scaled by the Biot tensor $\boldsymbol{b}$, whereas in the Terzaghi effective stress, the pressure term is scaled by the identity tensor $\mathbf{1}$. The elastic constitutive equation for the solid is given in terms of the Biot effective stress, whereas the dissipation inequality is defined in terms of the Terzaghi effective stress, i.e.,

$$\boldsymbol{\sigma}' = \mathbb{C}^e : \boldsymbol{\epsilon}^e\,, \qquad \boldsymbol{\sigma}'' : \dot{\boldsymbol{\epsilon}}^p \geq 0\,, \tag{2}$$

where $\mathbb{C}^e$ is the elastic moduli tensor of the solid matrix, and $\boldsymbol{\epsilon}^e$ and $\boldsymbol{\epsilon}^p$ are the elastic and plastic components of the strain in the solid.

Let K_s denote the bulk stiffness of the solid grains. The Biot tensor is given by

$$\boldsymbol{b} = \mathbf{1} - \frac{\mathbf{1} : \mathbb{C}^e}{3K_s} \equiv \mathbf{1} - \frac{\mathbb{C}^e : \mathbf{1}}{3K_s}\,. \tag{3}$$

In the limit of elastic isotropy, the Biot tensor reduces to the form

$$\boldsymbol{b} = \Big(1 - \frac{K}{K_s}\Big)\mathbf{1} = \alpha \mathbf{1}\,, \tag{4}$$

where K is the bulk stiffness of the solid matrix and $\alpha = (1 - K/K_s)$ is the Biot coefficient. Here, we allow the material to exhibit elastic anisotropy through the elasticity tensor $\mathbb{C}^e$.

The two effective stresses are obviously related through the equation

$$\boldsymbol{\sigma}'' = \boldsymbol{\sigma}' + (\mathbf{1} - \boldsymbol{b})\psi^w p\,, \tag{5}$$

so that $\boldsymbol{\sigma}'' = \boldsymbol{\sigma}'$ when $\boldsymbol{b} = \mathbf{1}$. Substituting the elastic constitutive equation for $\boldsymbol{\sigma}'$ then yields the equivalent elastic constitutive equation for $\boldsymbol{\sigma}''$ of the form

$$\boldsymbol{\sigma}'' = \mathbb{C}^e : \widetilde{\boldsymbol{\epsilon}}^e \,, \tag{6}$$

where

$$\widetilde{\boldsymbol{\epsilon}}^e = \boldsymbol{\epsilon}^e + \mathbb{C}^{e-1} : (\mathbf{1} - \boldsymbol{b})\psi^w p \tag{7}$$

is an equivalent elastic strain that defines the evolution of the Terzaghi effective stress $\boldsymbol{\sigma}''$. By setting $\widetilde{\boldsymbol{\epsilon}}^p = \boldsymbol{\epsilon}^p$ and

$$\widetilde{\boldsymbol{\epsilon}} = \widetilde{\boldsymbol{\epsilon}}^e + \widetilde{\boldsymbol{\epsilon}}^p \,, \tag{8}$$

an equivalent strain-driven plasticity theory can be developed in terms of the Terzaghi effective stress $\boldsymbol{\sigma}''$, which, at the same time, satisfies the elastic constitutive equation for the Biot effective stress $\boldsymbol{\sigma}'$.

2.2 Conservation laws

The balance of linear momentum can be written in terms of either the Biot effective stress or the Terzaghi effective stress. Because the plasticity theory is formulated in terms of the Terzaghi stress, we write the balance of linear momentum (ignoring inertia effects) in terms of this stress as follows

$$\nabla \cdot (\boldsymbol{\sigma}'' - \psi^w p \mathbf{1}) + \rho \boldsymbol{g} = \mathbf{0} \,, \tag{9}$$

where ρ is the total mass density of the solid-water-air mixture and $\boldsymbol{g}$ is the gravity acceleration vector. This expression is true whether the response is fully elastic or elastoplastic.

On the other hand, assuming no mass exchanges between water and the surrounding environment, the balance of mass for water takes the form

$$\psi^w(\boldsymbol{b} : \dot{\boldsymbol{\epsilon}}^e + \mathbf{1} : \dot{\boldsymbol{\epsilon}}^p) + c\dot{\psi}^w + \frac{\dot{p}}{\mathcal{M}} + \frac{1}{K_w}\nabla p \cdot \boldsymbol{q} + \nabla \cdot \boldsymbol{q} = 0 \,, \tag{10}$$

where K_w is the bulk modulus of water, $\boldsymbol{q}$ is the Darcy flux, and the superimposed dot is the material time derivative following the solid motion. The coefficient c is given by the expression

$$c = \phi + \frac{\beta}{K_s}\psi^w p \,, \tag{11}$$

in which

$$\beta = \frac{1}{3}\mathbf{1} : \boldsymbol{b} - \phi \,, \tag{12}$$

and ϕ is the porosity of the mixture; while $\mathcal{M}$ is the Biot modulus defined as

$$\frac{1}{\mathcal{M}} = \Big(\frac{\phi}{K_w} + \frac{\psi^w \beta}{K_s}\Big)\psi^w \,. \tag{13}$$

The balance of mass for air is not needed in this case since we have assumed the air pressure to be atmospheric.

2.3 Elastic anisotropy

In rocks with distinct bedding planes, the elastic response is often transversely isotropic [14, 39, 66]. The orientation of the plane of isotropy with respect to the horizontal can be defined by the microstructure tensor $\boldsymbol{m}$, which has the form

$$\boldsymbol{m} = \boldsymbol{n} \otimes \boldsymbol{n}\,, \tag{14}$$

where $\boldsymbol{n}$ is the unit normal vector to the plane of isotropy. For a transversely isotropic material the elasticity tensor is given by

$$\begin{aligned}\mathbb{C}^e = {} & \lambda \mathbf{1} \otimes \mathbf{1} + 2\mu_T \mathbb{I} + a(\mathbf{1} \otimes \boldsymbol{m} + \boldsymbol{m} \otimes \mathbf{1}) + b\boldsymbol{m} \otimes \boldsymbol{m} \\ & + (\mu_L - \mu_T)(\mathbf{1} \oplus \boldsymbol{m} + \boldsymbol{m} \oplus \mathbf{1} + \mathbf{1} \ominus \boldsymbol{m} + \boldsymbol{m} \ominus \mathbf{1})\,,\end{aligned} \tag{15}$$

where $\mathbb{I}$ is the rank-four symmetric identity tensor with components $I_{ijkl} = (\delta_{ik}\delta_{jl} + \delta_{jk}\delta_{il})/2$, and operators $\otimes$, $\oplus$ and $\ominus$ operate such that $(\boldsymbol{a} \otimes \boldsymbol{b})_{ijkl} = a_{ij}b_{kl}$, $(\boldsymbol{a} \oplus \boldsymbol{b})_{ijkl} = a_{jl}b_{ik}$, and $(\boldsymbol{a} \ominus \boldsymbol{b})_{ijkl} = a_{il}b_{jk}$ for any symmetric second-order tensors $\boldsymbol{a}$ and $\boldsymbol{b}$. The five parameters of the model, namely, λ, μ_L, μ_T, a, and b, characterize the transversely isotropic elastic material.

In terms of the five elasticity parameters, the Biot tensor for a transversely isotropic material can be written as

$$\boldsymbol{b} = b_\perp \boldsymbol{m} + b_\parallel (\mathbf{1} - \boldsymbol{m})\,, \tag{16}$$

where

$$b_\perp = 1 - \frac{3\lambda + 4a + b + 4\mu_L - 2\mu_T}{3K_s}\,, \qquad b_\parallel = 1 - \frac{3\lambda + 2\mu_T + a}{3K_s} \tag{17}$$

are the BN and BP components of this tensor.

Equivalently, the five parameters of the elasticity model can be represented by the Young's moduli of elasticity E_1 and E_2 in the BN and BP directions, respectively; Poisson's ratios ν_{12} and ν_{23}; and shear modulus G_{12}. In a recent paper [51], the authors have shown that these parameters vary with degree of saturation, with the stiffness moduli generally increasing with dehydration. They employed linear regression to express the variations of these parameters with saturation, and showed that an evolving anisotropy with saturation is crucial for capturing the observed responses of clay rocks during shrinkage tests. However, they have not considered the evolution of plastic anisotropy in their work, which is now the focus of the present paper.

2.4 Plastic anisotropy

To capture plastic anisotropy, we adopt the framework proposed by Semnani et al. [76] in which a fourth-rank projection tensor $\mathbb{P}$ rotates the Terzaghi effective stress tensor $\boldsymbol{\sigma}''$ to a fictitious stress configuration $\boldsymbol{\sigma}^*$ where the

yield surface can be written in isotropic form. The rotational transformation is given by

$$\boldsymbol{\sigma}^* = \mathbb{P} : \boldsymbol{\sigma}'' \,, \tag{18}$$

where

$$\begin{aligned}\mathbb{P} = c_1\mathbb{I} + \frac{c_2}{2}(\boldsymbol{m}\oplus\boldsymbol{m} + \boldsymbol{m}\ominus\boldsymbol{m}) \\ + \frac{c_3}{4}(\mathbf{1}\oplus\boldsymbol{m} + \mathbf{1}\oplus\mathbf{1} + \mathbf{1}\ominus\boldsymbol{m} + \boldsymbol{m}\ominus\mathbf{1})\end{aligned} \tag{19}$$

is the projection tensor. The anisotropy parameters c_1, c_2, and c_3 determine the aspect ratio of the yield surface, whereas the microstructure tensor $\boldsymbol{m}$ determines the rotation of the yield surface relative to the hydrostatic axis.

In the fictitious stress configuration, we consider a two-invariant yield criterion based on the isotropic modified Cam-Clay function of the form [17]

$$f(\boldsymbol{\sigma}^*, \bar{p}_c) = \frac{(q^*)^2}{M^2} + p^*\big(p^* - \bar{p}_c\big) \leq 0 \,, \tag{20}$$

where $p^* = \mathrm{tr}(\boldsymbol{\sigma}^*)/3$, $q^* = \sqrt{\frac{3}{2}}\|\boldsymbol{s}^*\|$, $\boldsymbol{s}^* = \boldsymbol{\sigma}^* - p^*\mathbf{1}$, M is the slope of the critical state line. In the real stress space,

$$p^* = \boldsymbol{a}^* : \boldsymbol{\sigma}'' \quad , \quad q^* = \sqrt{\tfrac{1}{2}}\,\|\boldsymbol{\sigma}''\|_{\mathbb{A}^*} \,, \tag{21}$$

where

$$\boldsymbol{a}^* = \mathbb{P} : \frac{1}{3}\mathbf{1} \,, \quad \|\boldsymbol{\sigma}''\|_{\mathbb{A}^*} = \sqrt{\boldsymbol{\sigma}'' : \mathbb{A}^* : \boldsymbol{\sigma}''} \,, \tag{22}$$

and

$$\mathbb{A}^* = \mathbb{P} : (3\mathbb{I} - \mathbf{1}\otimes\mathbf{1}) : \mathbb{P} \,. \tag{23}$$

By substituting these expressions into Equation (20), the yield function in the real stress space becomes

$$f(\boldsymbol{\sigma}'', \bar{p}_c) = \frac{\|\boldsymbol{\sigma}''\|^2_{\mathbb{A}^*}}{2M^2} + \boldsymbol{a}^* : \boldsymbol{\sigma}''(\boldsymbol{a}^* : \boldsymbol{\sigma}'' - \bar{p}_c) \leq 0 \,. \tag{24}$$

Note that the form of f in the real stress space is more complicated than in the fictitious stress space.

The size of the yield surface is determined by an effective preconsolidation stress, which has a functional relation given by

$$\bar{p}_c = \bar{p}_c(s, \psi^w, p_c) \,, \tag{25}$$

where $s = -p$ is the matric suction and p_c is the value of $\bar{p}_c$ when $s = 0$ (or when $\psi^w = 1$). Strictly speaking, either s or ψ^w in Equation (25) is redundant since there exists a constitutive relation between them, namely, the water retention law. The well-known van Genuchten equation [88] is one such law and is given by the curve

$$\psi^w = \psi_1 + \frac{\psi_2 - \psi_1}{[1 + (s/s_0)^n]^m}\,, \qquad m = 1 - \frac{1}{n}\,, \tag{26}$$

where ψ_1 and ψ_2 are the residual water saturation and maximum water saturation, respectively, s_0 is a scaling suction, and n and m are parameters describing the shape of the water retention curve.

The effect of partial saturation is to expand the yield surface from its size at the fully saturated state. The preconsolidation stress p_c at the fully saturated state varies with the plastic volumetric strain ε_v^p according to the equation

$$p_c = p_{c0} \exp(\vartheta \varepsilon_v^p)\,, \tag{27}$$

where ϑ is a coefficient that may depend on the degree of saturation as well, and p_{c0} is a reference value of p_c when $\varepsilon_v^p = 0$. We note that $p_c < 0$ and $p_{c0} < 0$ by the continuum mechanics convention. In the unsaturated state, the effective preconsolidation stress expands according to the equation

$$\bar{p}_c = -(-p_c)^b\,, \tag{28}$$

where $b \geq 1$. We note that this exponent typically increases with suction and approaches the value of one at zero suction. A specific form for b is given in the examples presented later in this paper.

Another effect of partial saturation is to reduce the compressibility of the rock and make it stiffer against volume change. In this work, we adopt the compressibility framework proposed by Sitarenios and Kavvadas [79] where the compression line depends on both suction and degree of saturation. The evolution law for compressibility is expressed as

$$\tilde{\lambda} = \tilde{\lambda}_0 \Big[1 - C(1 - \psi^w)^\gamma \Big(1 - e^{-Ds}\Big)\Big]\,, \tag{29}$$

where $\tilde{\lambda}_0$ is the compressibility of the rock at the fully saturated state; and C and D are positive constants similar to the parameters introduced by Alonso et al. [1]. In contrast to the bonding factor used in [15, 43], the effects of suction and degree of saturation on compressibility are independent of each other in this framework.

2.5 Evolution of plastic anisotropy

Semnani et al. [76] noted that the projection tensor $\mathbb{P}$ can be defined by the parameters, α, β, and γ when the coordinate system is aligned with the bedding planes, that is,

$$\begin{Bmatrix} \sigma_{11} \\ \sigma_{22} \\ \sigma_{33} \\ \sigma_{23} \\ \sigma_{13} \\ \sigma_{12} \end{Bmatrix}^* = \begin{bmatrix} \alpha & & & & & \\ & \beta & & & & \\ & & \beta & & & \\ & & & \beta & & \\ & & & & \gamma & \\ & & & & & \gamma \end{bmatrix} \begin{Bmatrix} \sigma_{11} \\ \sigma_{22} \\ \sigma_{33} \\ \sigma_{23} \\ \sigma_{13} \\ \sigma_{12} \end{Bmatrix}'' . \tag{30}$$

The parameters can be normalized by setting $\gamma = 1$. This means that the degree of plastic anisotropy can be represented by the values of α and β alone. These parameters can be regarded as the scaling factors of the stresses in and out of the bedding plane when projected to the fictitious stress space.

Similar to what was done to describe the evolution of elastic anisotropy with saturation [51], we now consider α and β to be linear functions of the degree of saturation and investigate their evolution with saturation. The evolution of plastic anisotropy can then be represented through four additional parameters:

$$\alpha = A_0 + A_1(1 - \psi^w)\,, \qquad \beta = B_0 + B_1(1 - \psi^w)\,, \tag{31}$$

where A_0 and B_0 are the values of α and β at the fully saturated state, respectively; and A_1 and B_1 are the slopes of α and β with the degree of saturation, respectively. In contrast to saturation-dependent elastic anisotropy, which was quantified from wave velocity measurements at different degrees of saturation [51], the four variable anisotropy parameters mentioned above must now be determined by fitting the full stress-strain experimental data of the anisotropic plastic responses at various degrees of saturation. The parameters A_0 and B_0 can be calibrated from the stress-strain curves in the BN and BP directions of a fully saturated sample [76]. Thereafter, A_1 and B_1 can be determined from the stress-strain curves in the BN and BP directions of unsaturated samples.

Figure 1 presents schematics of the evolution of the yield surface with degree of saturation in p^*-q^* and p-q space for different values of A_1 and B_1. Here, we assign an isotropic plastic response at full saturation (i.e., $A_0 = B_0 = 1$) and consider constant plastic anisotropy: (a) $A_1 = 0$ and $B_1 = 0$; as well as three cases of variable plastic anisotropy: (b) $A_1 = 0.4$ and $B_1 = 0$; (c) $A_1 = 0$ and $B_1 = -0.4$; and (d) $A_1 = 0.4$ and $B_1 = -0.4$.

Remark. We note that the anisotropy parameters, c_1, c_2, and c_3 of the projection tensor $\mathbb{P}$ can also be expressed as linear functions of the four variable anisotropy parameters introduced above, i.e.,

$$\left.\begin{aligned} c_1 &= B_0 + B_1(1 - \psi^w) \\ c_2 &= A_0 + B_0 - 2 + (A_1 + B_1)(1 - \psi^w) \\ c_3 &= 2 - 2B_0 - 2B_1(1 - \psi^w) \end{aligned}\right\}. \tag{32}$$

But throughout this paper, we focus instead on the variation of α and β with degree of saturation.

2.6 Implications for strength prediction

In this section, we elucidate the impacts on the predicted strengths of the rates A_1 and B_1 at which the anisotropy parameters α and β vary with the degree

of saturation. Under normally consolidated condition, the rock would undergo strain hardening during the loading stage, and so the compressive strength in this case is measured by the asymptotic value of the stress difference (or deviator stress) when an unsaturated sample is subjected to triaxial compression. To isolate the effect of plastic anisotropy on the mechanical responses, we assume elastic isotropy for now and explore the effect of the variable anisotropy properties on the evolution of the rock's compressive strength. The following material parameters are assumed: Young's modulus $E = 20,000$ MPa, Poisson's ratio $\nu = 0.25$. The plasticity parameters are selected as $\vartheta = 45$, $p_{c0} = 30$ MPa, $M = 1.2$, $C = 0.2$, $\gamma = 0.8$ and $D = 0.01$ kPa^{-1}. The water retention curve parameters are taken as $\psi_2 = 1.0$, $\psi_1 = 0.0$, $s_0 = 60$ MPa, $n = 1.84$, $m = 0.46$.

Figure 2 shows the trends in the evolution of rock strength with degree of saturation in the BN and BP directions. As expected, all strengths increase with dehydration. In addition, the curves for the isotropic material (Figure 2a) overlap since both the elastic and plastic responses are isotropic at all satu-

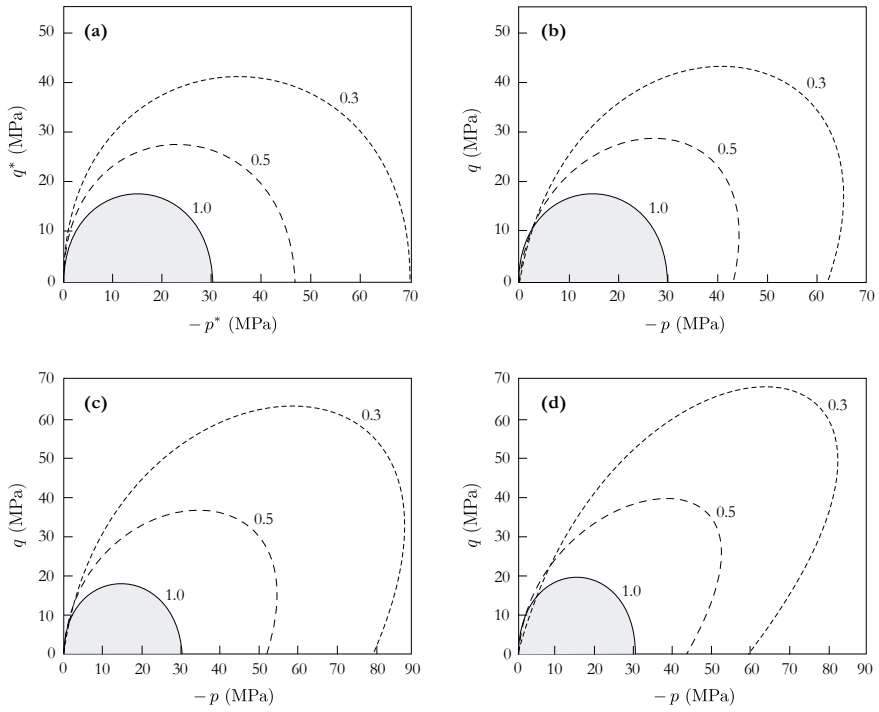

Fig. 1. Schematic representation of a transversely isotropic MCC model for unsaturated porous media in: (a) p^*-q^* space, and (b)–(d) p-q space. (b) $A_1 = 0.4$, $B_1 = 0$; (c) $A_1 = 0$, $B_1 = -0.4$; (d) $A_1 = 0.4$, $B_1 = -0.4$. Numbers next to the ellipses are values of degree of saturation ψ^w.

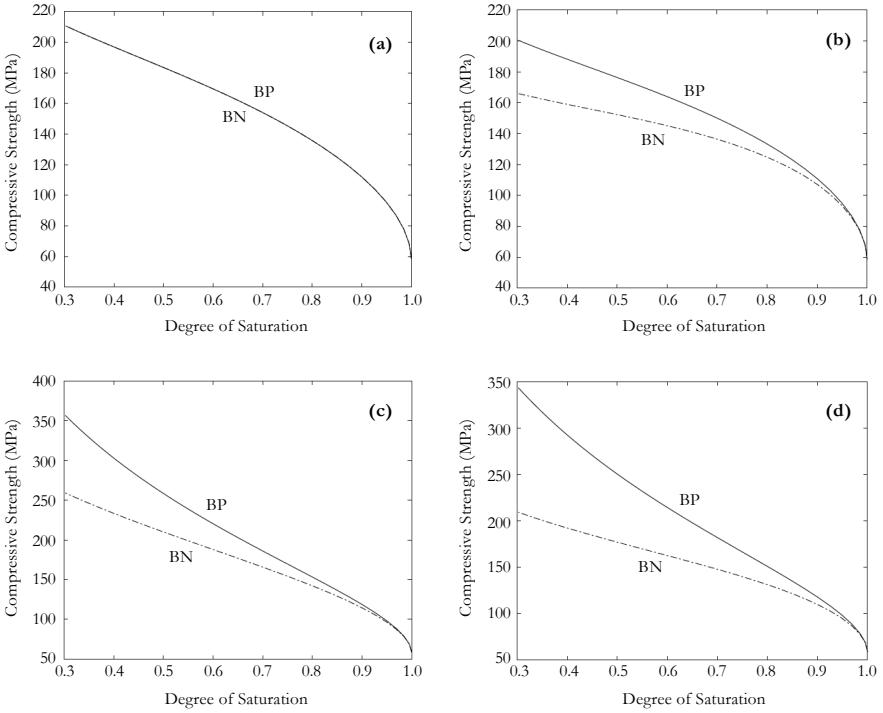

Fig. 2. Variation of triaxial compressive strength of normally consolidated clay rock with degree of saturation for different values of A_1 and B_1: (a) isotropic; (b) $A_1 = 0.4$, $B_1 = 0$; (c) $A_1 = 0$, $B_1 = -0.4$; (d) $A_1 = 0.4$, $B_1 = -0.4$.

ration levels. By comparison, increasing plastic anisotropy with dehydration results in different material strength curves in the BN and BP directions (Figures 2b,c,d). The value of B_1 appears to have a more significant effect on the BP strength and leads to a more significant increase at low saturation levels. Moreover, Figures 2c,d show larger increases in both BN and BP strengths as the material dehydrates, compared to Figure 2b, likely due to the value of B_1.

We also investigate the effect of the variable anisotropic parameters on the variation of material strength with bedding plane orientation. Figure 3 shows that not all values of A_1 and B_1 lead to realistic predictions. For example, Figure 3a shows that the rock gains in strength when the load is applied at an angle with respect to the bedding plane, an unrealistic trend that contradicts observed rock behavior (it is well known that the strength of transversely isotropic rocks is lowest between 20-40° inclination, see [54]). Similarly, Figure 3c shows that the minimum strength occurs in BN direction (bedding orientation of zero), which differs from the observed behavior of transversely isotropic rocks. On the other hand, Figure 3b results in U-shaped strength

anisotropy curves that are more similar to rock strength behavior reported in the literature [10, 14, 39, 62, 66, 70]. Thus, we see that certain combinations of the variable anisotropy parameters may give unreasonable curves of rock strength variation with bedding orientation, and so the shape of the strength-bedding orientation curve should also be considered when calibrating the anisotropy parameters.

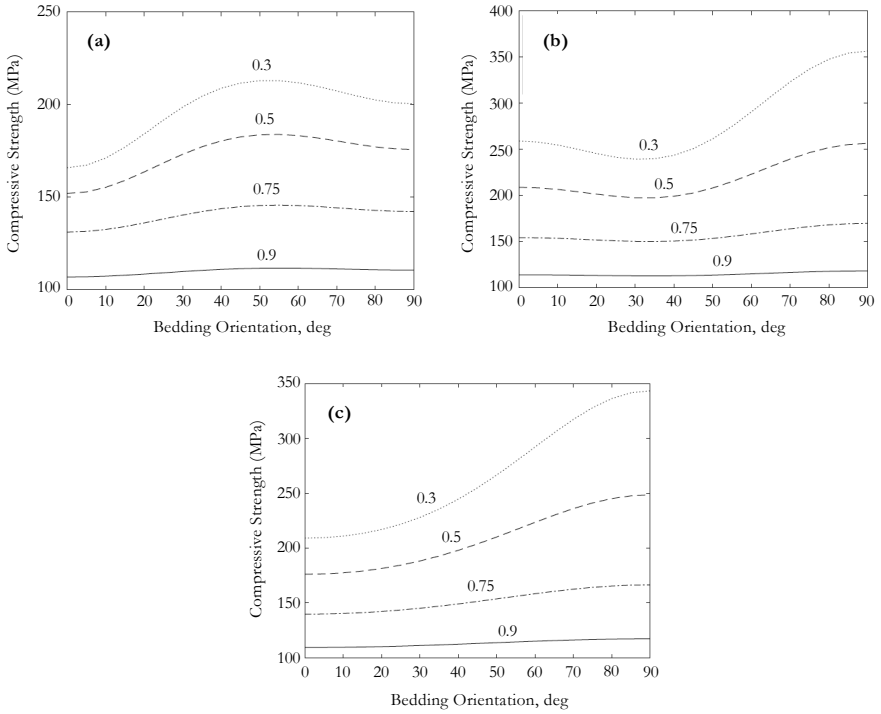

Fig. 3. Variation of triaxial compressive strength of normally consolidated clay rock with bedding plane orientation: (a) $A_1 = 0.4$, $B_1 = 0$; (b) $A_1 = 0$, $B_1 = -0.4$; (c) $A_1 = 0.4$, $B_1 = -0.4$. Numbers next to the curves are values of degree of saturation.

3 Tournemire shale

Experimental data demonstrating the dependence of elastic and plastic anisotropy on saturation are available in the literature for Tournemire shale [87]. In this section, we calibrate the model parameters against triaxial compression test data for this shale and investigate the evolution of the U-shaped anisotropy curves with degree of saturation. We should note that triaxial stress-strain data represent coupled elastic and plastic responses, so the plastic anisotropy

back-figured from the stress-strain curves is expected to depend on the elastic anisotropy to some extent. Following the simulations conducted by Semnani et al. [76], we replace $\boldsymbol{a}^*$ is Equation (24) with $\mathbf{1}/3$. It has been observed that this substitution provides a better match with the triaxial compression test data for Tournemire shale and suggests that only the deviatoric part of stress exhibits anisotropy for this shale.

3.1 Elastic anisotropy and water retention

Valès et al. [87] investigated the combined effects of degree of saturation and anisotropy on the mechanical behavior of Tournemire shale rock. They conducted de-saturation/re-saturation tests and triaxial compression tests with loading-unloading cycles at five saturation levels. From the stress-strain data, they reported measured values of the elasticity parameters for the transversely isotropic rock at five different degrees of saturation. We plot these values in Figure 4 and estimate their variations with degree of saturation by linear regression.

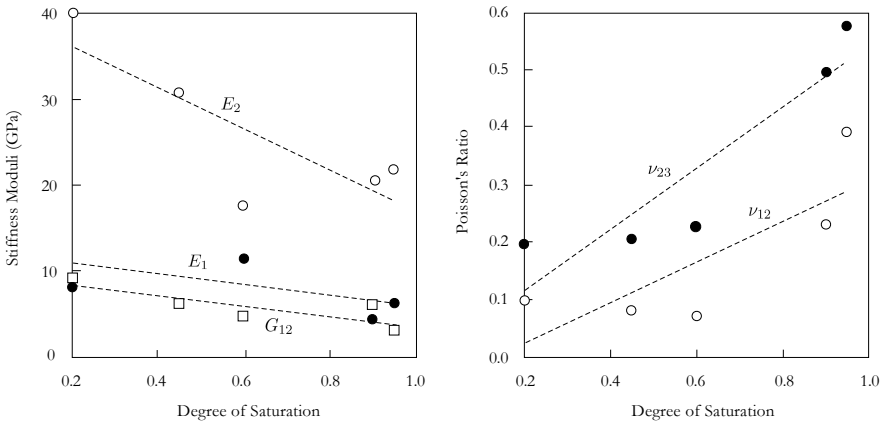

Fig. 4. Stiffness moduli (left) and Poisson's ratios (right) as functions of degree of saturation for Tournemire shale taken from Valès et al. [87]. Ticks are data points, dashed lines are estimated linear variations.

Let X denote an elastic parameter for a transversely isotropic rock (e.g. E_1, E_2, etc.). A linear function $X = X(\psi^w)$ with degree of saturation ψ^w can be represented by the equation [51]

$$X\left(\psi^w\right) = X_{\text{sat}} + \left(1.0 - \psi^w\right) a_X \,, \tag{33}$$

where X_{sat} is the value of X at full saturation (i.e. $\psi^w = 1$) and a_X is the slope of the straight-line variation with degree of saturation [51]. The values

of X_{sat} and a_X for the five elastic parameters for Tournemire shale are given in Table 1.

Table 1. Saturation-dependent elasticity parameters for Tournemire shale by linear regression. Experimental data from Valès et al. [87]. Note that E_1 is the stiffness modulus in the BN direction, E_2 in the BP direction.

Elastic parameter (X)	X_{sat}	a_X
E_1 (MPa)	6125	5972
E_2 (MPa)	17088	23894
G_{12} (MPa)	3574	6103
ν_{12}	0.307	−0.350
ν_{23}	0.542	−0.529

We back-figured the unsaturated plasticity model parameters for Tournemire shale using the strain evolution data from shrinkage tests. Table 2 summarizes these model parameters.The value of $\tilde{\lambda}_0$ was obtained from oedometric tests in the literature [67]. Additionally, the van Genuchten water retention parameters presented in Table 3 were obtained from results of Valès et al. where multiple identical samples were subjected to different suctions, and saturation was determined from water content and strain measurements.

Table 2. Unsaturated plasticity model parameters for Tournemire shale.

Parameter	Value
M	0.7
$\tilde{\lambda}_0$	0.0972
ϑ	140
γ	0.8
C	0.1
D (MPa^{-1})	1.05e−4

Table 3. Water retention parameters.

Parameter	Value
Maximum saturation, ψ_2	1.0
Residual saturation, ψ_1	0.0
Scaling pressure, s_0 (MPa)	62.9
Shape constant, n	1.84
Shape constant, m	0.46

3.2 Plastic anisotropy

Establishing the variations of the plastic anisotropy parameters α and β is less straightforward than performing a linear regression on the elasticity parameters. Whereas the elasticity parameters for the shale samples were given for each saturation, the plastic anisotropy parameters must be determined from the experimental stress-strain curves at different degrees of saturation.

Valès et al. [87] reported triaxial compression test data on Tournemire shale in the BN and BP directions at five degrees of saturation. No stress history was reported by the authors for the shale samples tested, so all samples were assumed to be normally consolidated in the simulations, with an initial confining pressure of 2.5 MPa. Triaxial compression tests were then simulated for each sample at the stress-point level by increasing the vertical strain while holding the lateral stresses fixed.

Figure 5 compares the experimental and simulated stress-strain curves at five degrees of saturation, namely, $\psi^w = 0.2$, 0.45, 0.6, 0.9, and 0.95. We first determined the anisotropy parameters α and β for each of the stress-strain curves by matching the experimental response for a given degree of saturation through a trial-and-error procedure. The corresponding estimated values of the anisotropy parameters are reported in Figure 6 and show a somewhat erratic trend in the variation of α and a monotonic decrease of β with saturation. In this case, a simple linear regression would predict the experimental stress-strain curves at some values of degree of saturation quite well, but would be too inaccurate for other values of degree of saturation. We thus adjusted the straight-line variations slightly (particularly the position of the straight line for β), and plot them as dashed lines in Figure 6. We note that more systematic techniques for model calibration, such as those presented in [22, 46, 100, 102], could also be utilized.

The dashed lines shown in Figure 6 are given by Equations (31) with $A_0 = 0.74$, $A_1 = 0.22$, $B_0 = 0.61$, and $B_1 = 0.43$. Because these lines do not pass through all the open circles shown in Figure 6, the predicted stress-strain curves do not perfectly match the experimental curves, as shown in Figure 7. In particular, we see that the initial slopes of some stress-strain curves were not predicted well (e.g. curves for $\gamma_w = 0.45$). This could be attributed to poor fit of the linear regressions on the variation of elastic moduli and Poisson's ratios with saturation. Nevertheless, these straight-line representations of α and β minimize the errors on the stress-strain curves over the entire range of saturation, and are considered sufficiently accurate for this example.

3.3 Implications for strength and volume change

Because the samples were assumed to be normally consolidated, the simulated stress-strain curves would approach the critical state asymptotically. The compressive strength can then be estimated as the asymptotic value of the deviator stress-axial strain curve at the critical state. Figure 8 portrays

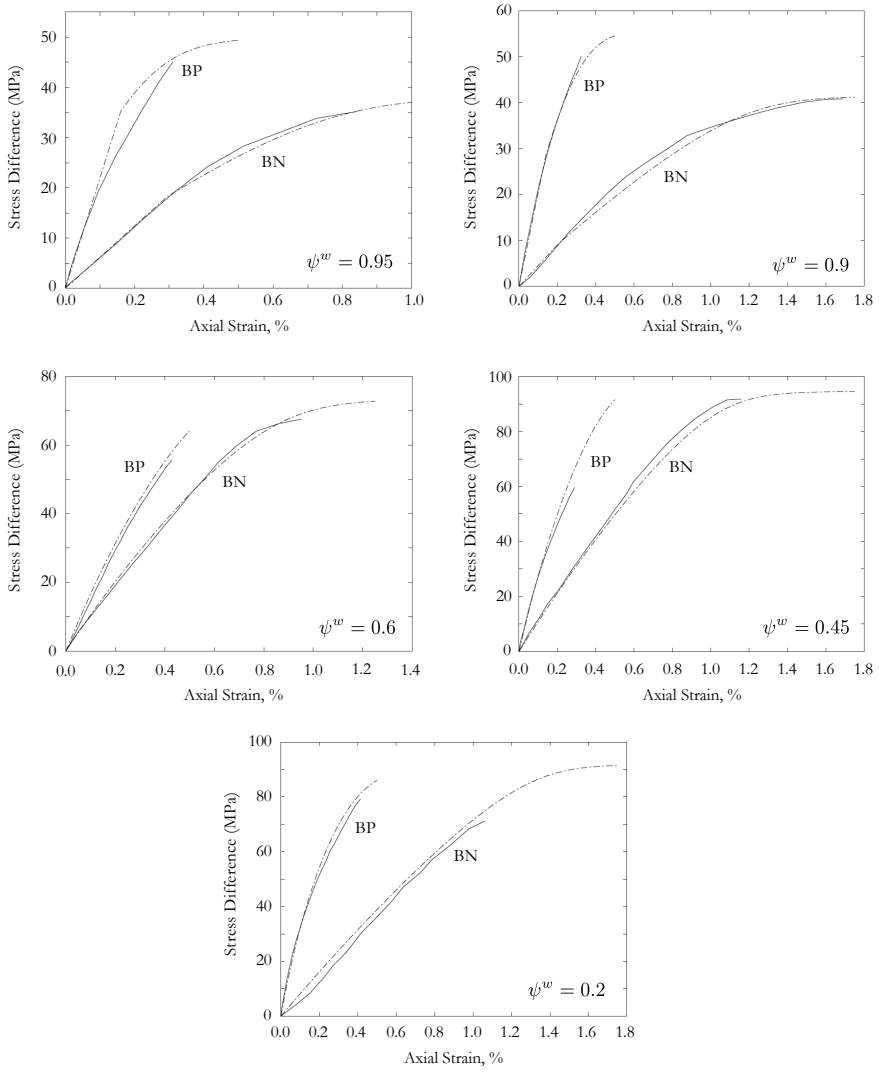

Fig. 5. Experimental [87] and simulated stress-strain responses of Tournemire shale at various degrees of saturation. For each degree of saturation, the plastic anisotropy parameters α and β were calibrated to match the experimental data. Solid curves = experiment; dashed curves = calibration.

the calculated compressive strengths as functions of bedding plane orientation and degree of saturation. All simulation results shown in this figure assume the calibrated linear variation with degree of saturation of the plastic anisotropy parameters α and β developed in the previous sections.

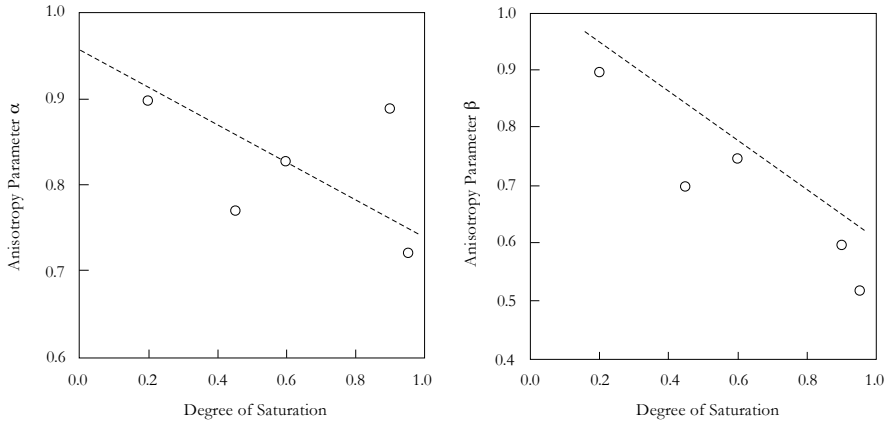

Fig. 6. Variations of anisotropy parameters α and β with saturation. Coordinates of the open circles are determined from Figure 5; dashed lines are estimated linear variations.

It can be observed that the shape and position of the compressive strength-bedding orientation curves evolve with degree of saturation. We see that the strength increases monotonically as the sample dehydrates. Furthermore, the U-shape variation is maintained for all values of degree of saturation, although the strength variation appears to exhibit a more isotropic behavior as the sample dehydrates (i.e., the U-shaped curve becomes flatter). This could be due to the effect of increasing confining pressure resulting from an increase in the suction stress as the sample dehydrates, which suppresses the effect of anisotropy. This trend is consistent with those reported by a number of authors [10, 62, 85, 106].

In Figure 9, we present the volumetric strains for triaxial compression tests in the BN and BP directions at saturation levels of $\psi^w = 0.45$ and 0.9. As expected, the volume change behavior depends on the orientation of the deviator load relative to the bedding plane, as well as on the degree of saturation at which the samples were tested. We see from the figure that the volumetric strain behavior in the BP direction is captured well by the proposed model. The initial volume change behavior in the BN direction is also captured well; however, the test results show subsequent dilative behavior at larger values of deviator stress, which was not replicated by the model.

The dilative behavior described above suggests that the rock samples tested could in fact be overconsolidated, even though the authors [87] did not report the stress histories for the samples. At $\psi^w = 0.45$, note that the sample also began to exhibit a dilative behavior right before the completion of the test. This dilative behavior could be due to both the bulk constitutive response resulting from overconsolidation and the dilative response within the zones of localized deformation.

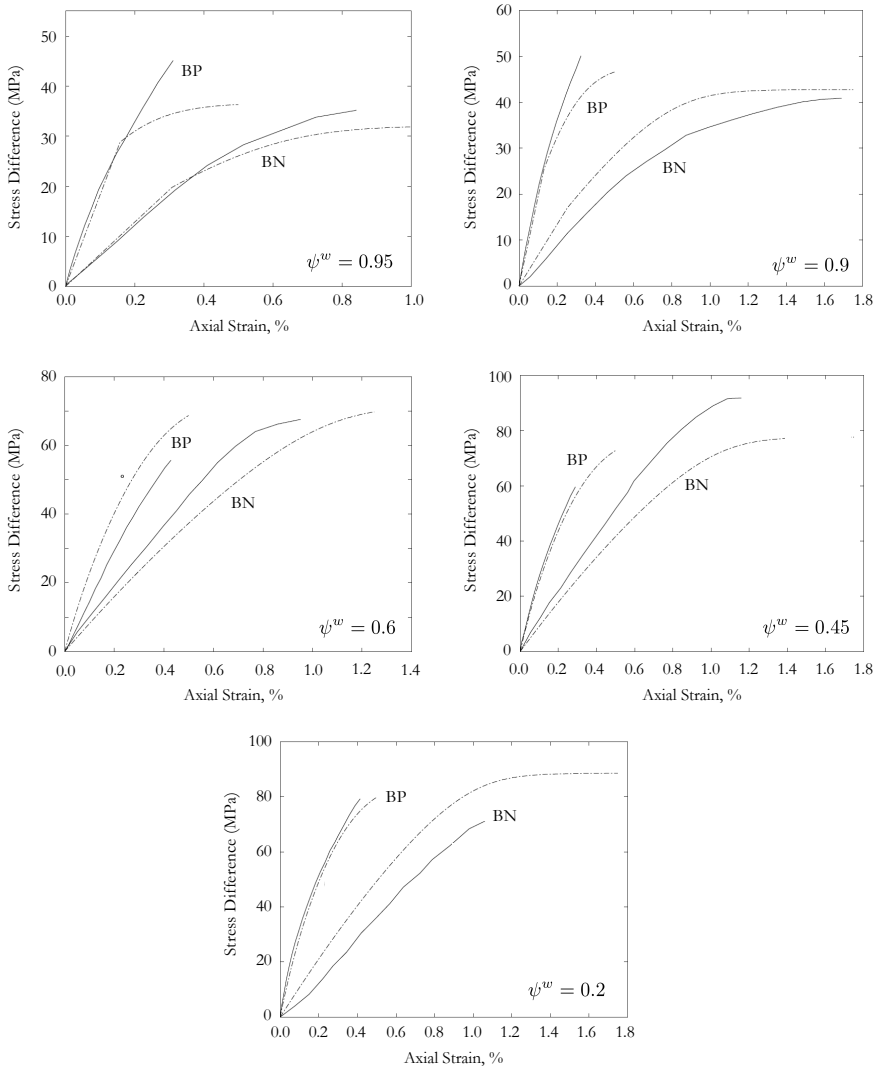

Fig. 7. Experimental [87] and predicted stress-strain responses of Tournemire shale at various degrees of saturation. Predictions use linear variations of the plastic anisotropy parameters α and β, with $A_0 = 0.74$, $A_1 = 0.22$, $B_0 = 0.61$, and $B_1 = 0.43$. Solid curves = experiment; dashed curves = prediction.

3.4 Wetting-induced swelling of Tournemire shale

Wetting tests were simulated for a normally consolidated specimen under a confining pressure of 200 MPa and a deviatoric stress of 220 MPa. The suction of the specimen was decreased at a constant rate from 400 MPa to 20

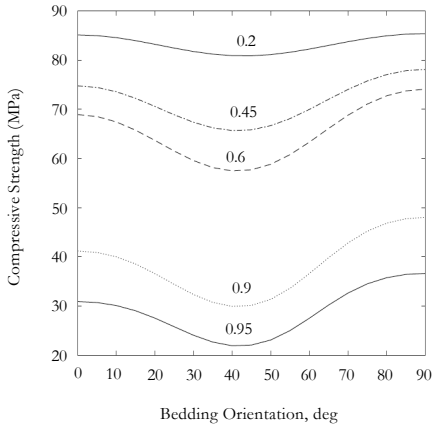

Fig. 8. Variation of compressive strength with bedding orientation for Tournemire shale. Numbers next to the curves are degrees of saturation.

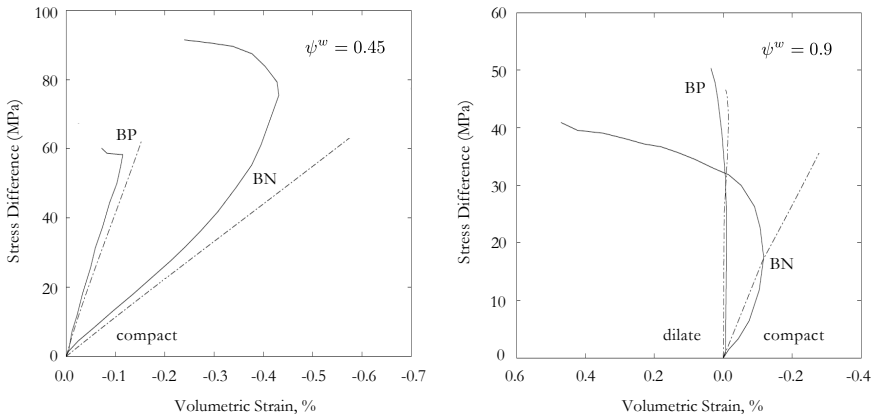

Fig. 9. Deviator stress versus volumetric strain curves for Tournemire shale under triaxial compression at degrees of saturation $\psi^w = 0.45$ (left) and $\psi^w = 0.9$ (right).

MPa, which corresponds to an increase in the degree of saturation from 20% to 95%. Three cases of material behavior and parameters were considered: (i) variable plastic anisotropy parameters given in Section 3.2; (ii) constant plastic anisotropy with $\alpha = 0.92$ and $\beta = 0.95$ obtained from linear regression at $\psi^w = 0.2$; and (iii) purely elastic behavior by assigning a very large preconsolidation pressure. Comparisons between the plastic and purely elastic cases allows us to differentiate between the effects of elastic anisotropy and those of plastic anisotropy.

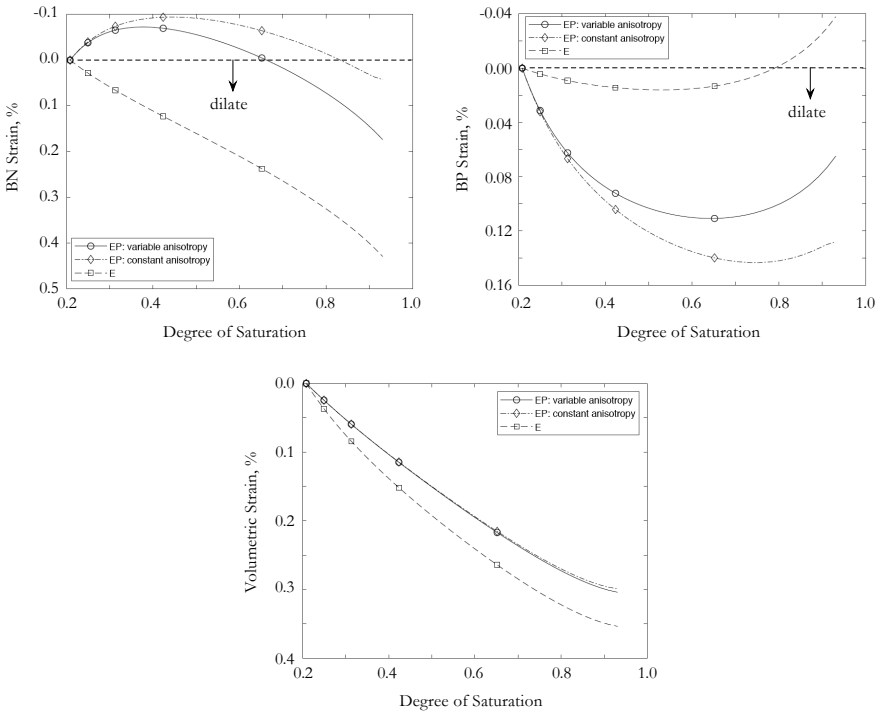

Fig. 10. Anisotropic wetting-induced swelling of Tournemire shale under a confining pressure of 200 MPa and deviator stress of 220 MPa. E = elastic, EP = elastoplastic.

Figure 10 presents the simulated strains in the BN and BP directions as well as the volumetric strains induced by wetting of all three material behaviors for a deviatoric stress of 220 MPa. For the elastoplastic cases, the specimen compacts slightly in the BN direction when the saturation level starts to increase before dilating at higher saturation levels. On the other hand, the BP strains are always dilative, but do not increase monotonically with the degree of saturation. Still, the volumetric strains are always dilative. Comparing the elastoplastic cases, we observe that the variable anisotropy case has more swelling in the BN direction and less swelling in the BP direction than the constant anisotropy case. This difference in behavior is in part due to increasing plastic anisotropy upon wetting. The β-term decreases at a faster rate than the α-term upon saturation, which causes the ratio α/β to increase from 0.96 at $\psi^w = 0.2$ to 1.19 at $\psi^w = 0.95$. However, both cases predict very similar volumetric strains since the same compressibility parameters are used.

Upon comparison with the purely elastic case, we can deduce that non-monotonic evolution of strains in the BP and BN directions are likely caused by different mechanisms. The decrease in dilative strains in the BP direction can be attributed to elastic anisotropy as the same behavior is also observed

in the purely elastic case. On the other hand, compaction in the BN direction could be due to wetting-collapse behavior when the saturation increases. The results indicate that variable plastic anisotropy can substantially influence the mechanical behavior of clay rocks during wetting under high deviatoric loads. This would have implications on the applications of these clay rocks where there is significant change in the degree of saturation, such as the construction of tunnels and underground repositories.

4 Shear bands with variable anisotropy

This section presents a boundary-value problem simulating plane strain compression of rectanglar specimens. The numerical simulations were conducted in Geocentric, a massively parallel finite-element code for geomechanics [92]. It is built on the deal.II finite-element library [8, 11], p4est mesh handling library [20], and the Trilinos project [47].

We simulated plane strain compression on rectangular specimens under globally undrained but locally drained conditions. This implies that fluid is allowed to flow within the sample but is prevented from entering or leaving through the exterior boundaries of the sample. The specimens measure 75 mm tall and 37 mm wide and were modeled with 760 stabilized mixed finite elements with equal-order linear interpolation for displacement and pressure fields [30, 93]. To eliminate the effect of variable elastic anisotropy, and thus, highlight the effect of plastic anisotropy, constant transversely isotropic elastic parameters were adopted: $E_1 = 9.3$ GPa, $E_2 = 24.2$ GPa, $\nu_{12} = 0.27$, $\nu_{23} = 0.2$ and $G_{12} = 3.9$ GPa. These values are approximately the same as those obtained for Tournemire shale [71, 72]. The Biot tensor is characterized by the components $b_\perp = 0.57$ and $b_\parallel = 0.36$. The plasticity model parameters calibrated for Tournemire shale in Section 3.2 were used. The permeabilities were taken as $\kappa_\parallel = 10^{-19}$ m^2 and $\kappa_\perp = 10^{-20}$ m^2. We assume the same planes of isotropy for both the hydraulic and mechanical behavior.

The top and bottom edges of the mesh were supported on vertical rollers, except at the bottom corner node that was pinned for stability. The samples were subjected to an initial confining pressure of $\sigma_c = 10$ MPa at an initial preconsolidation pressure of $p_c = -30$ MPa. Vertical compression of the samples were conducted at a strain rate of 0.2%/min. We imposed an inhomogeneous initial field condition in the form of a spatially varying degree of saturation. Figure 11 shows the initial degree of saturation, which was generated by a random function generator employing a normal distribution, with a mean value ($\bar{\psi}^w$) of 0.9, standard deviation of 0.016 and a range of [0.83,0.96]. The spatial variation of the plastic parameters, α and β are also presented in Figure 11. As a consequence of a spatially inhomogeneous degree of saturation, the suction and the effective stresses also vary within the specimen and create an initially inhomogeneous stress field. The variable suction also creates a pressure gradient field that induces fluid flow within the specimen.

To establish a statically admissible initial condition, the first load step is used to iteratively balance the internal (effective stresses and pore pressures) and external (applied confining pressure) forces.

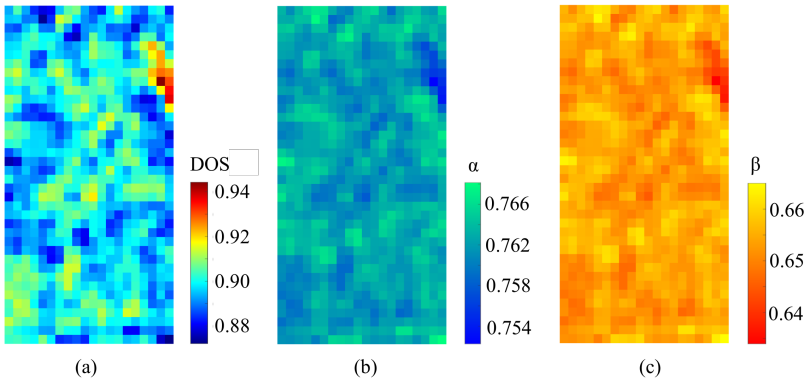

Fig. 11. Random distributions of initial conditions: (a) degree of saturation (DOS); and plastic parameters (b) α and (c) β. The mean value of the random distribution is $\bar{\psi}^w = 0.9$.

Figures 12a and 13a present the localized zones of deformation that develop in two samples with different bedding plane orientations ($\theta = 15°, 60°$) at an axial compression of 2.5%. We observed that for $\theta = 60°$, the zone of localized deformation is much more diffuse than for $\theta = 15°$. The equivalent plastic strains that develop for $\theta = 60°$ are also larger. This can be attributed to the variation of compressive strength with bedding orientation and degree of saturation. At $\psi_w = 0.9$, the compressive strength of Tournemire shale at $\theta = 60°$ is smaller than at $\theta = 15°$ from Figure 8. The contours of the degree of saturation are shown in Figures 12b and 13b. The variation of degree of saturation smoothens out over time when compared to the initial spatial variation. The effect of bedding plane orientation are clearly reflected in the resulting contours of degree of saturation. Fluid flow in the BP direction is more significant due to a larger BP permeability. Similarities between the equivalent plastic strain and pore pressure contours are observed for the bedding plane orientation $\theta = 60°$. The zone of localized deformation generally coincides with higher saturation levels, due to more compaction within the zone of localized deformation [18]. In comparison, the zone of localized deformation does not coincide with higher saturation levels for $\theta = 15°$.

We also conducted the same simulations at a lower degree of saturation for comparison. The random distribution of initial saturation presented in Figure 11 was shifted to a mean of $\bar{\psi}^w = 0.45$ while keeping the same standard deviation. The spatial variation of these new initial conditions are presented in Figure 14. Both plastic parameters α and β increase throughout the specimen.

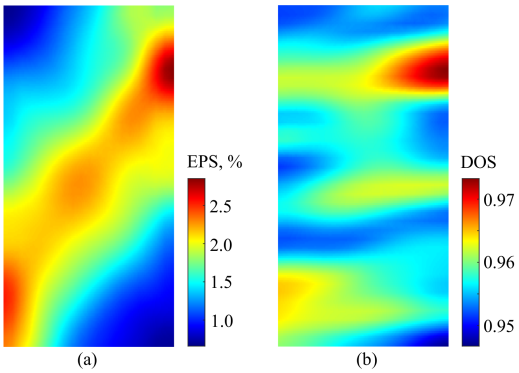

Fig. 12. Contours of (a) equivalent plastic strain $\|\boldsymbol{\epsilon}^p\|$ (EPS) and (b) degree of saturation (DOS) at an axial strain of 2.5% at $\bar{\psi}^w = 0.9$ and bedding plane angle $\theta = 15°$

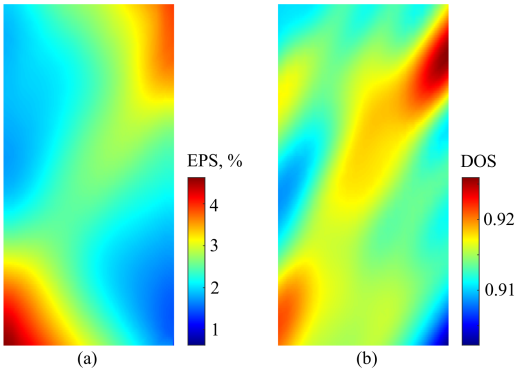

Fig. 13. Contours of (a) equivalent plastic strain $\|\boldsymbol{\epsilon}^p\|$ (EPS) and (b) degree of saturation (DOS) at an axial strain of 2.5% at $\bar{\psi}^w = 0.9$ and bedding plane angle $\theta = 60°$

We note that there is less plastic anisotropy at a lower degree of saturation. The average ratio of α/β throughout the specimen decreases from 1.16 in Figure 11 to 1.02 in Figure 14.

The plastic strains that develop at a lower average degree of saturation ($\bar{\psi}^w = 0.45$) are substantially different from at $\bar{\psi}^w = 0.9$. They are smaller due to higher compressive strength at lower saturation levels. In the case of $\theta = 15°$, the zone of localized deformation occurs at the lower left corner with a slight V-shape configuration and does not reach the top half of the specimen. The localized deformation that develops for $\theta = 60°$ is less smooth than its counterpart at $\bar{\psi}^w = 0.9$. This can be attributed to the more erratic variation of saturation. At lower saturation levels, fluid flow is impeded by lower relative permeabilities, which increase the time required for the saturation contours

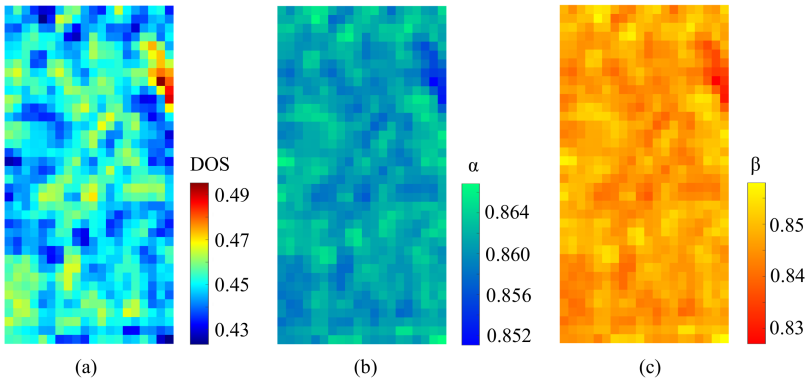

Fig. 14. Random distributions of initial conditions: (a) degree of saturation (DOS); and plastic parameters (b) α and (c) β. The mean value of the random distribution is $\bar{\psi}^w = 0.45$.

to smoothen out. As a result, the saturation contours comprise many pockets of low and high saturation throughout the sample. A similar behavior of rock specimens fracturing with rougher fracture surfaces at lower saturation levels has been previously observed and reported in Bure claystone [59].

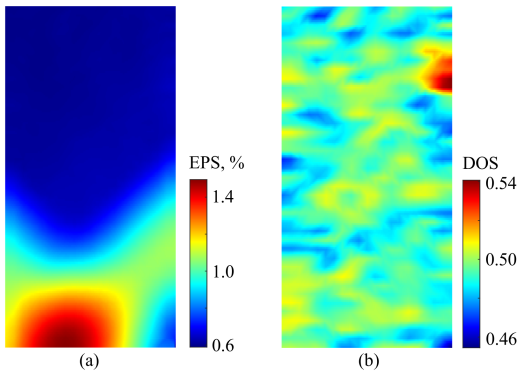

Fig. 15. Contours of (a) equivalent plastic strain $\|\boldsymbol{\epsilon}^p\|$ (EPS) and (b) degree of saturation (DOS) at an axial strain of 2.5% at $\bar{\psi}^w = 0.45$ and bedding plane angle $\theta = 15^\circ$

A unique aspect of the anisotropic framework presented in this study is the use of two effective stresses associated with the elastic and plastic strain rates. We compare the J_2 invariant of the two effective stresses. Figure 17 presents the contours of the difference between their J_2 invariant (ie. $J_{2\sigma''} - J_{2\sigma'}$) for bedding plane angles of $\theta = 15^\circ$ and 60° at an average saturation levels of

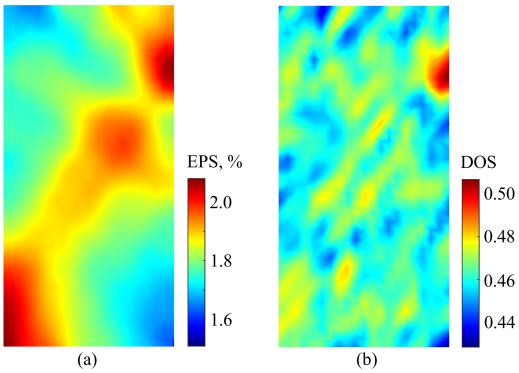

Fig. 16. Contours of equivalent plastic strain $\|\boldsymbol{\epsilon}^p\|$ (EPS) and degree of saturation (DOS) at an axial strain of 2.5% at $\bar{\psi}^w = 0.45$ and bedding plane angle $\theta = 60^\circ$

$\bar{\psi}^w = 0.9$. The difference between the two effective stresses differs significantly with the bedding plane orientation. In the sample with bedding plane angles of $\theta = 60^\circ$, the contour of stress difference is very similar to the saturation contours in Figure 13. The contour for $\theta = 15^\circ$ instead shows similarities to the contours of the equivalent plastic strain. Additionally, the J_2 invariant of σ'' is larger than that of σ' when $\theta = 60^\circ$. However, this relationship flips when $\theta = 15^\circ$. The effect of the Biot tensor on the effective stress tensors changes substantially with the bedding plane orientation.

Figure 18 shows the contours of the stress difference at an average saturation levels of $\bar{\psi}^w = 0.45$. The contours differ substantially from those at $\bar{\psi}^w = 0.9$. They are much more erratic, similar to the fluctuating saturation contours for $\bar{\psi}^w = 0.45$. The contours for both bedding plane angles are similar to their respective saturation contours. We also observe that the stress difference is larger for $\theta = 60^\circ$ by about an order of magnitude. Thus, the Biot tensor has a larger effect on the effective stresses at higher bedding plane orientations which in turn would affect the elastoplastic strains that develop.

5 Conclusion

We have presented an anisotropic elastoplastic framework for unsaturated porous media that accounts for the combined effects of saturation and transverse isotropy. The formulation adopts two effective stress measures: the Biot effective stress $\boldsymbol{\sigma'}$ that is conjugate to the elastic strain, and the Terzaghi effective stress $\boldsymbol{\sigma''}$ that is conjugate to the plastic strain. For the plastic mechanical response, we extended the anisotropic MCC model proposed in Semnani et al. [76] to the unsaturated regime incorporating the compressibility framework proposed by Sitarenios & Kavvadas [79]. We have also introduced evolving anisotropy in the plastic constitutive model. The components of the

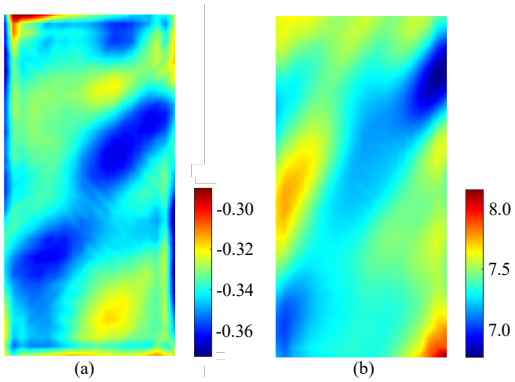

Fig. 17. Contours of the difference between the two effective stress measures ($J_{2\sigma''} - J_{2\sigma'}$) at $\bar{\psi}^w = 0.9$ for bedding plane angles (a) $\theta = 15°$; and (b) $\theta = 60°$ at an axial strain of 2.5%. Color bars are stress difference in MPa.

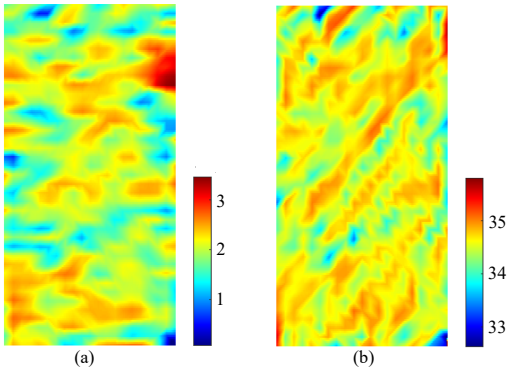

Fig. 18. Contours of the difference between the two effective stress measures $[J_2(\sigma'') - J_2(\sigma')]$ at $\bar{\psi}^w = 0.45$ for bedding plane angles (a) $\theta = 15°$; and (b) $\theta = 60°$, at an axial strain of 2.5%. Color bars are stress difference in MPa.

fourth-order projection tensor $\mathbb{P}$ are defined as linear functions of the degree of saturation to capture an evolving anisotropic plastic yield surface. Furthermore, the elastic moduli are assumed to evolve linearly with saturation following Ip et al. [51]. The model has been calibrated using experimental data from Valès et al. [87] for Tournemire shale at various saturation levels.

The numerical results demonstrate that the proposed framework is capable of capturing the anisotropic mechanical behavior of unsaturated rocks at various saturation levels. Simulations of wetting test suggest that evolving plastic anisotropy has substantial influence on the anisotropic mechanical behavior during wetting under large deviatoric stresses. Neglecting its effects may result in inaccurate predictions of the mechanical behavior in rocks experiencing wetting and drying processes. Additionally, we have investigated

the combined effects of material anisotropy and degree of saturation on the mechanical and fluid flow responses in plane strain compression simulations under globally undrained conditions using the proposed framework.

Data availability statement

The datasets generated during the course of this study are available from the corresponding author upon reasonable request.

References

[1] Alonso EE, Gens A, Josa A (1990). A constitutive model for partially saturated soils. Géotechnique 40(3):405–430.
[2] Al-Harthi AA (1998). Effect of planar structures on the anisotropy of Ranyah sandstone, Saudi Arabia. Engineering geology 50(1–2):49–57.
[3] Al-Sharrad MA, Gallipoli D (2014 June). An elasto-plastic model for unsaturated soils with evolving anisotropy. In Proceedings of the 6th International Conference on Unsaturated Soils UNSAT, pp. 433–439.
[4] Al-Sharrad MA, Gallipoli D (2016). Incorporating anisotropy in the Barcelona Basic Model. E3SWeb Conf, 9:17003.
[5] Al-Sharrad MA, Gallipoli D, Wheeler SJ (2017). Experimental investigation of evolving anisotropy in unsaturated soils. Géotechnique 67(12):1033–1049.
[6] Amadei B (1996, April). Importance of anisotropy when estimating and measuring in situ stresses in rock. In International Journal of Rock Mechanics and Mining Sciences & Geomechanics Abstracts 33(3):293–325.
[7] Amorosi A, Rollo F, Houlsby GT (2020). A nonlinear anisotropic hyperelastic formulation for granular materials: comparison with existing models and validation. Acta Geotechnica 15:179–196.
[8] Arndt D, Bangerth W, Blais B, Clevenger TC, Fehling M, Grayver AV, Heister T, Heltai L, Kronbichler M, Maier M, Munch P, Pelteret J, Rastak R, Tomas I, Tuurcksin B, Wang Z, Wells D (2020). The deal. II library, version 9.2. Journal of Numerical Mathematics 28(3):131–146.
[9] Ashworth M, Doster F (2020). Anisotropic dual-continuum representations for multiscale poroelastic materials: Development and numerical modelling. International Journal for Numerical and Analytical Methods in Geomechanics 44(17):2304–2328.
[10] Attewell PB, Sandford MR (1974, November). Intrinsic shear strength of a brittle, anisotropic rock—I: experimental and mechanical interpretation. In International Journal of Rock Mechanics and Mining Sciences & Geomechanics Abstracts 11(11):423–430.

[11] Bangerth W, Hartmann R, Kanschat G (2007). deal. II—A general-purpose object-oriented finite element library. ACM Transactions on Mathematical Software (TOMS) 33(4): 24-es.
[12] Baud, P., Louis, L., David, C., Rawling, G. C., & Wong, T. F. (2005). Effects of bedding and foliation on mechanical anisotropy, damage evolution and failure mode. Geological Society, London, Special Publications 245(1):223–249.
[13] Bennett KC, Berla LA, Nix WD, Borja RI (2015) Instrumented nanoindentation and 3D mechanistic modeling of a shale at multiple scales. Acta Geotechnica 10:1–14
[14] Bonnelye A, Schubnel A, David C, Henry P, Guglielmi Y, Gout C, Fauchille AL, Dick P (2017). Strength anisotropy of shales deformed under uppermost crustal conditions. Journal of Geophysical Research: Solid Earth 122(1):110–129.
[15] Borja RI (2004). Cam-Clay plasticity, Part V: A mathematical framework for three-phase deformation and strain localization analyses of partially saturated porous media. Computer Methods in Applied Mechanics and Engineering 193(48–51):5301–5338
[16] Borja RI (2006). On the mechanical energy and effective stress in saturated and unsaturated porous continua. International Journal of Solids and Structures 43(6):1764–1786.
[17] Borja RI (2013). Plasticity Modeling & Computation, Spinger, Berlin-Heidelberg.
[18] Borja RI, Song X, & Wu W (2013). Critical state plasticity. Part VII: Triggering a shear band in variably saturated porous media. Computer Methods in Applied Mechanics and Engineering 261: 66–82.
[19] Borja RI, Yin Q, Zhao Y (2020). Cam-Clay plasticity. Part IX: On the anisotropy, heterogeneity, and viscoplasticity of shale. Computer Methods in Applied Mechanics and Engineering 360:112695.
[20] Burstedde C, Wilcox LC, Ghattas O (2011). p4est: Scalable algorithms for parallel adaptive mesh refinement on forests of octrees. SIAM Journal on Scientific Computing 33:1103–1133.
[21] Cai G, Zhou A, Liu Y, Xu R, Zhao C (2020). Soil water retention behavior and microstructure evolution of lateritic soil in the suction range of 0–286.7 MPa. Acta Geotechnica 15: 3327–3341.
[22] Calvello M, Finno RJ (2004). Selecting parameters to optimize in model calibration by inverse analysis. Computers and Geotechnics 31(5):410–424.
[23] Camargo JT, White JA, Castelleto N, Borja RI (2021). Preconditioners for multiphase poromechanics with strong capillarity. International Journal for Numerical and Analytical Methods in Geomechanics 45(9):1141–1168.
[24] Cao Z, Chen J, Alonso EE, Tarragona AR, Cai Y, Gu C, Zhang Q (2021). A constitutive model for the accumulated strain of unsaturated soil under high-cycle traffic loading. International Journal

for Numerical and Analytical Methods in Geomechanics 45:990–1004, https://doi.org/10.1002/nag.3188

[25] Chen Y, Yang Z (2019). A bounding surface model for anisotropically overconsolidated clay incorporating thermodynamics admissible rotational hardening rule. International Journal for Numerical and Analytical Methods in Geomechanics 44(5):668–690.

[26] Chen Y, Buscarnera G (2021). Numerical simulation of unstable suction transients in unsaturated soils: the role of wetting collapse. International Journal for Numerical and Analytical Methods in Geomechanics 45:1569–1587.

[27] Cheng AHD (2020). A linear constitutive model for unsaturated poroelasticity by micromechanical analysis. International Journal for Numerical and Analytical Methods in Geomechanics 44(4):455–483.

[28] Cho JW, Kim H, Jeon S, Min KB (2012). Deformation and strength anisotropy of Asan gneiss, Boryeong shale, and Yeoncheon schist. International journal of rock mechanics and mining sciences (1997) 50:158–169.

[29] Choo J, Semnani SJ, White JA (2021). An anisotropic viscoplasticity model for shale based on layered microstructure homogenization. International Journal for Numerical and Analytical Methods in Geomechanics 45(4):502–520.

[30] Choo J, Borja RI (2015). Stabilized mixed finite elements for deformable porous media with double porosity. Computer Methods in Applied Mechanics and Engineering 293:131–154.

[31] Crook AJ, Yu JG, Willson SM (2002, January). Development of an orthotropic 3D elastoplastic material model for shale. In SPE/ISRM Rock Mechanics Conference. Society of Petroleum Engineers.

[32] Dafalias YF (1986). An anisotropic critical state soil plasticity model. Mechanics Research Communications 13(6):341–347

[33] Dafalias YF. An anisotropic critical state clay plasticity model. In Constitutive Laws for Engineering Materials:Theory and Applications, Proceedings of 2nd IC, vol. I, Desai CS et al. (eds). Elsevier: New York, 1987; 513–521.

[34] Dafalias, YF, Manzari MT, Papadimitriou AG. (2006). SANICLAY: simple anisotropic clay plasticity model. International Journal for Numerical and Analytical Methods in Geomechanics 30(12):1231–1257.

[35] Dejaloud H, Rezani, M (2021). Adaptive anisotropic constitutive modeling of natural clays. International Journal for Numerical and Analytical Methods in Geomechanics 45:1756–1790, https://doi.org/10.1002/nag.3223

[36] DeReuil AA, Birgenheier LP, McLennan J (2019). Effects of Anisotropy and Saturation on Geomechanical Behavior of Mudstone. Journal of Geophysical Research: Solid Earth 124(8):8101–8126.

[37] Dewhurst DN, Siggins AF (2006). Impact of fabric microcracks and stress field on shale anisotropy. Geophysical Journal International 165(1):135–148.
[38] D'Onza F, Gallipoli D, Wheeler SJ (2010). Effect of anisotropy on the prediction of unsaturated soil response under triaxial and oedometric conditions. Unsaturated soils 2:787–794.
[39] Donath FA (1961). Experimental study of shear failure in anisotropic rocks. Geological Society of America Bulletin 72(6):985-989.
[40] Douma LA, Dautriat J, Sarout J, Dewhurst DN, Barnhoorn A (2020). Impact of water saturation on the elastic anisotropy of the Whitby Mudstone, United Kingdom. Geophysics 85(1):MR57–MR72.
[41] Faizi SA, Kwok CY, Duan K (2020). The effects of intermediate principle stress on the mechanical behavior of transversely isotropic rocks: Insights from DEM simulations. International Journal for Numerical and Analytical Methods in Geomechanics 44(9):1262–1280.
[42] Feng K, Huang D, Wang G (2021). Two-layer material point method for modeling soil–water interaction in unsaturated soils and rainfall-induced slope failure. Acta Geotechnica. https://doi.org/10.1007/s11440-021-01222-9
[43] Gallipoli D, Gens A, Sharma R, Vaunat J (2003). An elasto-plastic model for unsaturated soil incorporating the effects of suction and degree of saturation on mechanical behaviour. Géotechnique 53(1):123–135.
[44] Ghaffaripour O, Esgandani GA, Khoshghalb A, Shahbodaghkhan B (2019). Fully coupled elastoplastic hydro-mechanical analysis of unsaturated porous media using a meshfree method. International Journal for Numerical and Analytical Methods in Geomechanics 43(11):1919–1955.
[45] Han B, Cai G, Zhou A, Li J, Zhao C (2021). A bounding surface model for unsaturated soils considering the microscopic pore structure and interparticle bonding effect due to water menisci. Acta Geotechnica 16:1331–1354.
[46] Hashash YM, Fu Q, Ghaboussi J, Lade PV, Saucier C (2009). Inverse analysis–based interpretation of sand behavior from triaxial compression tests subjected to full end restraint. Canadian Geotechnical Journal 46(7):768–791.
[47] Heroux MA, Willenbring JM (2012). A new overview of the Trilinos project. Scientific Programming 20(2):83–88.
[48] Hornby BE, Schwartz LM, Hudson JA (1994). Anisotropic effective-medium modeling of the elastic properties of shales. Geophysics, 59:1570–1583.
[49] Hu D, Zhou H, Zhang F, Shao J, Zhang J (2013). Modeling of inherent anisotropic behavior of partially saturated clayey rocks. Computers and Geotechnics 48:29–40.
[50] Hu H, Braun P, Delage P, Ghabezloo S (2021). Evaluation of anisotropic poroelastic properties and permeability of the Opalinus Clay using a single transient experiment. Acta Geotechnica 16:2131–2142.

[51] Ip SCY, Choo J, Borja RI (2021). Impacts of saturation-dependent anisotropy on the shrinkage behavior of clay rocks. Acta Geotechnica, https://doi.org/10.1007/s11440-021-01268-9.
[52] Johnston JE, NI Christensen (1995). Seismic anisotropy of shales. Journal of Geophysical Research 100:5991–6003.
[53] Kavvadas M (1982). Non-linear consolidation around driven piles in Clays. Cambridge, MA.
[54] Khanlari G, Rafiei B, Abdilor Y (2015). Evaluation of strength anisotropy and failure modes of laminated sandstones. Arabian Journal of Geosciences 8(5):3089–3102.
[55] Li D, Wong LNY, Liu G, Zhang X (2012). Influence of water content and anisotropy on the strength and deformability of low porosity meta-sedimentary rocks under triaxial compression. Engineering Geology 126:46–66.
[56] Li K, Yin ZY, Cheng Y, Cao P, Meng J (2020). Three-dimensional discrete element simulation of indirect tensile behaviour of a transversely isotropic rock. International Journal for Numerical and Analytical Methods in Geomechanics 44(13):1812–1832.
[57] Li Y, Zhang W, Zhang R (2021). Numerical investigation on performance of braced excavation considering soil stress-induced anisotropy. Acta Geotechnica, https://doi.org/10.1007/s11440-021-01171-3
[58] Liu C, Abousleiman Y (2020). Generalized solution to the anisotropic Mandel's problem. International Journal for Numerical and Analytical Methods in Geomechanics, 44(17):2283–2303.
[59] Liu Z, Shao J (2016). Moisture effects on damage and failure of Bure claystone under compression. Géotechnique Letters 6(3):182–186.
[60] Ma T, Wei C, Yao C, Yi P (2020). Microstructural evolution of expansive clay during drying-wetting cycle. Acta Geotechnica 15: 2355–2366.
[61] Maedo M, Sánchez M, Aljeznawi D, Manzoli O, Guimarães LJ, Cleto PR (2020). Analysis of soil drying incorporating a constitutive model for curling. Acta Geotechnica 15:2619–2635.
[62] McLamore R, Gray KE (1967). The mechanical behavior of anisotropic sedimentary rocks. Journal of Engineering for Industry 89(1):62–73.
[63] Mishra PN, Zhang Y, Bhuyan MH, Scheuermann A (2020). Anisotropy in volume change behaviour of soils during shrinkage. Acta Geotechnica 15:339–3414.
[64] Ni H, Liu J, Guo J, Yang D, Chen Y (2020). Numerical modelling on water retention and permeability of compacted GMZ bentonite under free-swelling conditions. International Journal for Numerical and Analytical Methods in Geomechanics 44(12):1619–1633.
[65] Nova R (1980, December). The failure of transversely isotropic rocks in triaxial compression. In International Journal of Rock Mechanics and Mining Sciences & Geomechanics Abstracts (Vol. 17, No. 6, pp. 325–332). Pergamon.

[66] Niandou H, Shao JF, Henry JP, Fourmaintraux D (1997). Laboratory investigation of the mechanical behaviour of Tournemire shale. International Journal of Rock Mechanics and Mining Sciences 34(1): 3–16.
[67] Noiret A, Giot R, Bemer E, Giraud A, Homand F (2011). Hydromechanical behavior of Tournemire argillites: measurement of the poroelastic parameters and estimation of the intrinsic permeability by œdometric tests. International Journal for Numerical and Analytical Methods in Geomechanics 35(4):496–518.
[68] Papadimitriou AG, Chaloulos YK, Dafalias YF (2019) A fabric-based sand plasticity model with reversal surfaces within anisotropic critical state theory. Acta Geotechnica 14: 253–277.
[69] Petalas AL, Dafalias YF, Papadimitriou AG (2019) SANISAND-FN: An evolving fabric-based sand model accounting for stress principal axes rotation. International Journal for Numerical and Analytical Methods in Geomechanics 43: 97–123.
[70] Ramamurthy T (1993). Strength and modulus responses of anisotropic rocks. Compressive Rock Engineering 1(13):313–329.
[71] Ramambasoa N, Rejeb A, Minh DN (2000, July). Hydromechanical behavior of shales-Application to the Tournemire site, France. In 4th North American Rock Mechanics Symposium. OnePetro.
[72] Rejeb A, Cabrera J (2004). DECOVALEX-THMC, description for task C, excavation disturbed zone (EDZ) in the argillaceous Tournemire site (France). Technical report, Institute of Radioprotection and Nuclear Safety (IRSN), France.
[73] Rojas E, Horta J, Pérez-Rea ML, Hernández CE (2019). A fully coupled simple model for unsaturated soils. International Journal for Numerical and Analytical Methods in Geomechanics 43(6):1143–1161.
[74] Romero E, Jommi C (2008). An insight into the role of hydraulic history on the volume changes of anisotropic clayey soils. Water Resources Research 44(5)a:W12412, doi:10.1029/2007WR006558.
[75] Rotisciani GM, Desideri A, Amorosi A (2021). Unsaturated structured soils: constitutive modelling and stability analyses. Acta Geotechnica, https://doi.org/10.1007/s11440-021-01313-7
[76] Semnani SJ, White JA, Borja RI (2016). Thermoplasticity and strain localization in transversely isotropic materials based on anisotropic critical state plasticity. International Journal for Numerical and Analytical Methods in Geomechanics 40(18):2423–2449.
[77] Shi HL, Hosdez J, Rougelot T, Xie SY, Shao JF, Talandier J (2021). Influences of structural anisotropy and heterogeneity on three-dimensional strain fields and cracking patterns of a clay-rich rock. Acta Geotechnica 16:2175–2187.
[78] Sitarenios P, Kavvadas, M. (2014). A compressibility framework to describe the volume change behaviour of unsaturated clayey soils. Unsaturated Soils: Research & Applications, 1:449.

[79] Sitarenios P, Kavvadas M (2020). A plasticity constitutive model for unsaturated, anisotropic, nonexpansive soils. International Journal for Numerical and Analytical Methods in Geomechanics 44(4):435-4-54.
[80] Soe AKK, Osada M, Takahashi M, Sasaki T (2009). Characterization of drying-induced deformation behaviour of Opalinus Clay and tuff in no-stress regime. Environmental Geology 58(6):1215–1225.
[81] Sone H, Zoback MD (2013). Mechanical properties of shale-gas reservoir rocks—Part 1: Static and dynamic elastic properties and anisotropy. Geophysics 78(5):D381–D392.
[82] Song X, Borja RI (2014). Mathematical framework for unsaturated flow in the finite deformation range. International Journal for Numerical Methods in Engineering 14(9):658–682.
[83] Song X, Borja RI (2014). Finite deformation and fluid flow in unsaturated soils with random heterogeneity. Vadose Zone Journal 13(5), DOI: 10.2136/vzj2013.07.0131.
[84] Stropeit K, Wheeler S, Cui YJ (2008). An anisotropic elasto-plastic model for unsaturated soils. Unsat Soils Adv Geo-Eng, 625–631.
[85] Su X, Nguyen S, Haghighat E, Pietruszczak S, Labrie D, Barnichon JD, Abdi H (2017). Characterizing the mechanical behaviour of the Tournemire argillite. Geological Society, London, Special Publications 443(1):97–113.
[86] Ueda K, Iai S (2019) Constitutive modeling of inherent anisotropy in a strain space multiple mechanism model for granular materials. International Journal for Numerical and Analytical Methods in Geomechanics 43:708–737
[87] Valès F, Minh DN, Gharbi H, Rejeb A (2004). Experimental study of the influence of the degree of saturation on physical and mechanical properties in Tournemire shale (France). Applied Clay Science 26(1-4):197–207.
[88] Van Genuchten MT (1980). A closed-form equation for predicting the hydraulic conductivity of unsaturated soils. Soil Science Society of America Journal 44(5):892–898.
[89] Vaunat J, Romero E, Jommi C (2000). An elastoplastic hydromechanical model for unsaturated soils. In A. Tarantino & C. Mancuso, Experimental evidence and theoretical approaches in unsaturated soils (91–106). CRC Press.
[90] Vecchia GD, Romero E (2013). A fully coupled elastic–plastic hydromechanical model for compacted soils accounting for clay activity. International Journal for Numerical and Analytical Methods in Geomechanics 37(5):503–535.
[91] Wheeler SJ, Näätänen A, Karstunen M, Lojander M (2003). An anisotropic elastoplastic model for soft clays. Canadian Geotechnical Journal 40(2):403–418.

[92] White JA, Borja RI (2011). Block-preconditioned Newton-Krylov solvers for fully coupled flow and geomechanics. Computational Geosciences 15:647–659.
[93] White JA, Borja RI (2008). Stabilized low-order finite elements for coupled solid-deformation/fluid-diffusion and their application to fault zone transients. Computer Methods in Applied Mechanics and Engineering 197(49–50):4353–4366.
[94] Xiao Y, Zhang Z, Wang J (2020). Granular hyperelasticity with inherent and stress-induced anisotropy. Acta Geotechnica 15:671–680.
[95] Xiong YL, Ye GL, Xie Y, Ye B, Zhang S, Zhang F (2019) A unified constitutive model for unsaturated soil under monotonic and cyclic loading. Acta Geotechnica 14: 313–328.
[96] Xu G, Gutierrez M, He C, Wang S (2021). Modeling of the effects of weakness planes in rock masses on the stability of tunnels using an equivalent continuum and damage model. Acta Geotechnica 16:2143–2164.
[97] Yamakawa Y, Hashiguchi K, Sasaki T, Higuchi M, Sato K, Kawai T, Machishima T, Iguchi T (2021). Anisotropic subloading surface Cam-clay plasticity model with rotational hardening: Deformation gradient-based formulation for finite strain. International Journal for Numerical and Analytical Methods in Geomechanics, https://doi.org/10.1002/nag.3268
[98] Yin Q, Liu Y, Borja RI (2021). Mechanisms of creep in shale from nanoscale to specimen scale. Computers and Geotechnics 136:104138
[99] Yurikov A, Lebedev M, Pervukhina M, Gurevich B (2019). Water retention effects on elastic properties of Opalinus shale. Geophysical Prospecting 67(4):984–996.
[100] Zentar R, Hicher PY, Moulin G. (2001). Identification of soil parameters by inverse analysis. Computers and Geotechnics 28(2):129–144.
[101] Zhang F, Xie SY, Hu DW, Shao JF, Gatmiri B (2012). Effect of water content and structural anisotropy on mechanical property of claystone. Applied Clay Science 69:79–86.
[102] Zhang Y, Gallipoli D, Augarde C (2013). Parameter identification for elasto-plastic modelling of unsaturated soils from pressuremeter tests by parallel modified particle swarm optimization. Computers and Geotechnics 48: 293–303.
[103] Zhang Q, Choo J, Borja RI (2019). On the preferential flow patterns induced by transverse isotropy and non-Darcy flow in double porosity media. Computer Methods in Applied Mechanics and Engineering 353:570–592.
[104] Zhang Q, Fan X, Chen P, Ma T, Zeng F (2020). Geomechanical behaviors of shale after water absorption considering the combined effect of anisotropy and hydration. Engineering Geology 269:105547.

[105] Zhang Q (2020). Hydromechanical modeling of solid deformation and fluid flow in the transversely isotropic fissured rocks. Computers and Geotechnics 128:103812.
[106] Zhang Q, Fan X, Chen P, Ma T, Zeng F (2020). Geomechanical behaviors of shale after water absorption considering the combined effect of anisotropy and hydration. Engineering Geology 269:105547.
[107] Zhang Q, Borja RI (2021). Poroelastic coefficients for anisotropic single and double porosity media. Acta Geotechnica 16:3013–3025.
[108] Zhao NF, Ye WM, Chen B, Chen YG, Cui YJ (2019) Modeling of the swelling–shrinkage behavior of expansive clays during wetting–drying cycles. Acta Geotechnica 14:1325–1335.
[109] Zhao Y, Semnani SJ, Yin Q, Borja RI (2018). On the strength of transversely isotropic rocks. International Journal for Numerical and Analytical Methods in Geomechanics 42(16):1917–1934.
[110] Zhao Y, Borja RI (2020). A continuum framework for coupled solid deformation-fluid flow through anisotropic elastoplastic porous media. Computer Methods in Applied Mechanics and Engineering 369:113225.
[111] Zhao Y, Borja RI (2021). Anisotropic elastoplastic response of double-porosity media. Computer Methods in Applied Mechanics and Engineering 380:113797.